○ **Earth, Planets and Space**

FULL PAPER

Open Access

Modelling of electromagnetic signatures of global ocean circulation: physical approximations and numerical issues

Libor Šachl[1,2]* ⬤, Zdeněk Martinec[1,2], Jakub Velímský[1], Christopher Irrgang[3], Johannes Petereit[3], Jan Saynisch[3], David Einšpigel[1,2] and Neesha Regmi Schnepf[4]

Abstract

The interactions of flowing electrically conductive seawater with Earth's magnetic field generate electric currents within the oceans, as well as secondary electric currents induced in the resistive solid Earth. The ocean-induced magnetic field (OIMF) is an observable signature of these currents. Ignoring tidally forced ocean flows, the global ocean circulation system is driven by wind forcing on the ocean surface and by the temperature- and salinity-dependent buoyancy force. Ocean circulation's magnetic signals contribute to the total magnetic field observed at the Earth's surface or by low-orbit satellite missions. In this paper, we concentrate on accurate numerical modelling of the OIMF employing various approaches. Using a series of numerical test cases in different scenarios of increasing complexity, we evaluate the applicability of the unimodal thin-sheet approximation, the importance of galvanic coupling between the oceans and the underlying mantle (i.e. the bimodal solution), the effects of vertical stratification of ocean flow as well as the effects of vertical stratification of both oceanic and underlying electrical conductivity, and the influence of electromagnetic self-induction. We find that the inclusion of galvanic ocean-mantle coupling has the largest effect on the predicted OIMF. Self-induction is important only on the largest spatial scales, influencing the lowest spherical harmonic coefficients of the OIMF spectrum. We find this conclusion important in light of the recent Swarm satellite mission which has the potential to observe the large-scale OIMF and its seasonal variations. The implementation of fully three-dimensional ocean flow and conductivity heterogeneity due to bathymetry, which substantially increases the computational demands of the calculations, can play some role for regional studies, or when a more accurate OIMF prediction is needed within the oceans, e.g. for comparison with seafloor observations. However, the large-scale signals at the sea surface or at satellite altitude are less affected.

Keywords: EM induction, Wind-driven ocean circulation, Approximation

Introduction

In this paper, we are concerned with modelling the ocean-induced magnetic field (OIMF) due to the wind- and buoyancy-driven ocean circulation; tides are considered separately in a companion paper by Velímskýet al. (2018). In particular, we inspect how various commonly used approximations affect the accuracy of modelled OIMF.

Interest in OIMF has been raised by the pioneering works of Cox et al. (1970), Sanford (1971), Sanford (1982), and Larsen and Sanford (1985). The first attempts to numerically model the OIMF were by Stephenson and Bryan (1992) and Flosadóttir et al. (1997), who used ocean currents from the Geophysical Fluid Dynamics Laboratory (GFDL) ocean model, and Tyler et al. (1997), who used The Ocean and isoPYCnal coordinates (OPYC, Oberhuber 1993a, b) ocean currents. Vivier et al. (2004) attempted quantifying the magnitude of the OIMF forced by electric currents from the Océan PArallélisé (OPA, Madec et al. 1998), Hamburg Ocean Primitive Equation (HOPE, Marsland et al. 2003) and Estimating the

*Correspondence: sachl@karel.troja.mff.cuni.cz
[1] Department of Geophysics, Faculty of Mathematics and Physics, Charles University, V Holešovičkách 2, 180 00 Praha 8, Czech Republic
Full list of author information is available at the end of the article

Šachl *et al. Earth, Planets and Space*   (2019) 71:58

Page 2 of 13

Circulation and Climate of the Ocean (ECCO, Marshall et al. 1997) models at the CHAMP satellite altitude of 400 km. Manoj et al. (2006) studied the magnetic field induced by ocean electric currents from the ECCO and Ocean Circulation and Climate Advanced Modelling project (OCCAM, Webb et al. 1998) models both at the sea level and the Swarm lower satellite-pair altitude of 430 km. All studies found a small (≈ 1 nT) signal at satellite height with the Antarctic Circumpolar Current (ACC) producing the largest signal because of its substantial water transport (it is the largest ocean current on Earth) and proximity to the geomagnetic pole.

The most consistent approach for calculating the OIMF is based on full three-dimensional (3-D) electromagnetic (EM) modelling where electric conductivity and ocean electric currents vary with lateral coordinates as well as with depth. However, the above-mentioned papers follow an alternative approach which relies on vertically integrating the ocean electric conductivity and electric currents. The effect of both quantities' vertical stratification is thus lost. The ocean model is forced by fluxes of momentum due to wind stress, heat, and fresh water (Large and Yeager 2004, 2009). All of these fluxes enter the ocean via its surface. The transport and diffusive processes are then responsible for the distribution of surface fluxes into the whole ocean volume. Consequently, ocean circulation is not two-dimensional (2-D), and it has a complex vertical structure. This is in contrast to tidal circulation which is predominantly barotropic due to low variations of the tidal force in the vertical direction within the ocean. Velímský et al. (2019) demonstrated the importance of the toroidal magnetic field generated by vertically stratified flows, as well as the galvanic coupling between the ocean and mantle.

A commonly used modelling simplification is the neglect of both EM self-induction in the ocean and mutual induction with the underlying mantle. This effect can be safely neglected when the horizontal spatial scale is much smaller than the penetration depth. In the case of seasonal variations, the penetration depth is in the range of thousands of kilometres, and hence, OIMF variations on comparable scales will be affected. Additionally, global ocean circulation is a nonlinear dynamic system with turbulent features such as eddies and jets. Self-induction in the oceans will be important for the mesoscale induced OIMF (i.e. spatial scales below 10 km, and time scales from days to weeks), provided both the ocean model and magnetic field model have sufficient spatio-temporal resolution to resolve these features.

Practical motivation for our study comes from the ongoing geomagnetic field measuring satellite mission, Swarm. Swarm has provided new knowledge about Earth and its electromagnetic environment (Olsen et al.

2016); however, one of the declared objectives of the mission—detecting magnetic signatures due to ocean circulation (Friis-Christensen et al. 2006)—has not yet been achieved. Such an accomplishment is a challenging task. Firstly, the OIMF is rather small, up to 2 nT at the satellite height, and it is overlaid by larger contributions ($\approx 50,000$ nT) from the main magnetic field and the magnetic fields of ionosphere and magnetosphere origin. Secondly, unlike the tidal magnetic signature, there is no single dominant frequency for ocean circulation and the process is instead relatively slow with a typical time scale of weeks. The ocean-induced magnetic field may thus be erroneously attributed to the lithospheric field which is stationary in time and has comparable magnitudes. Nonetheless, if the ocean-induced contribution is one day reliably isolated from satellite magnetic data, such satellite measurements could constrain ocean dynamics by coupling models of ocean circulation and ocean-induced magnetic fields (Irrgang et al. 2017). Accurate and efficient forward (and inverse) modelling is necessary for this breakthrough.

This study aims to fill the gap in the literature by inspecting the impact of galvanic coupling using unimodal and bimodal solutions, vertical stratification of ocean flow and electrical conductivity, self-induction and horizontal resolution on the numerically predicted OIMF. The unimodal solution considers only the poloidal magnetic field mode, and there is no galvanic coupling between the ocean and the underlying mantle. The bimodal solution contains both the toroidal and poloidal magnetic field modes. The toroidal magnetic mode is generated by poloidal electric currents which galvanically couple the ocean with the mantle.

The paper is organized as follows. We introduce the governing equations for the EM induction modelling and describe the EM induction solvers used in the study. We continue with a detailed description of our test cases and modelling set-up. We then present our results and conclusions.

Modelling of OIMF

The OIMF $\mathbf{B}(\mathbf{r}, t)$ obeys the quasi-static Maxwell equations supplemented by Ohm's law,

$$\nabla \cdot \mathbf{B} = 0, \tag{1}$$

$$\nabla \times \mathbf{B} = \mu_0 \left(\mathbf{j} + \mathbf{j}^{\mathrm{imp}} \right), \tag{2}$$

$$\nabla \times \mathbf{E} = -\frac{\partial \mathbf{B}}{\partial t}, \tag{3}$$

$$\mathbf{j} = \sigma \mathbf{E}, \tag{4}$$

Šachl *et al. Earth, Planets and Space* (2019) 71:58

Page 3 of 13

where $\mathbf{E}(\mathbf{r}, t)$ is the electric field, $\mathbf{j}(\mathbf{r}, t)$ is the electric current density, $\mathbf{j}^{\mathrm{imp}}(\mathbf{r}, t)$ is the imposed electric current density, $\sigma(\mathbf{r})$ is the electric conductivity, μ_0 is the permeability of vacuum, $\mathbf{r}$ is the radius vector, and t is time.

Alternatively, we can combine Eqs. (2)–(4) into the second-order EM induction equation for the OIMF,

$$\nabla \times \left(\frac{1}{\sigma} \nabla \times \mathbf{B} \right) + \mu_0 \frac{\partial \mathbf{B}}{\partial t} = \mu_0 \nabla \times \mathbf{E}^{\mathrm{imp}}, \qquad (5)$$

where $\mathbf{E}^{\mathrm{imp}}(\mathbf{r}, t)$ is the imposed electric field that is linked to the imposed electric current density through Ohm's law.

Note that Eqs. (2), (3) and (5) implicitly assume that the main geomagnetic field $\mathbf{B}_M(\mathbf{r}, t)$ is a potential field and its temporal variations are much slower than the temporal variations of the OIMF.

We compute the imposed electric field or electric currents from the ocean velocity $\mathbf{u}(\mathbf{r}, t)$ and the main geomagnetic field, following:

$$\mathbf{E}^{\mathrm{imp}} = \mathbf{j}^{\mathrm{imp}}/\sigma = \mathbf{u} \times \mathbf{B}_M, \qquad (6)$$

where we assume that the main geomagnetic field is much stronger than the OIMF.

In this paper, we use three EM induction solvers: the ElmgTD, X3DG and UTSM. All of them were thoroughly tested; ElmgTD and X3DG took part in the benchmark study of Kelbert et al. (2014) and were used to model OIMF in the past (Manoj et al. 2006; Irrgang et al. 2016b; Velímský et al. 2019). The main characteristics of individual solvers are summarized in Table 1. Each solver uses a different modelling technique—including different spatial discretizations and different ways to propagate dependent variables in time. Additionally, each solver was developed independently; the authors' teams do not overlap. Thus, we believe that our conclusions are not biased by choices specific to one particular solver. In the following text, we briefly describe the ElmgTD, X3DG and UTSM solvers.

ElmgTD solver

ElmgTD (Velímský and Martinec 2005; Velímský 2013) solves the EM induction equation (5) using a time-domain, spherical harmonic-finite element approach.

The recent version of ElmgTD employs the Crank–Nicolson time integration scheme, enforces the divergence-free condition on the magnetic field by means of Lagrange-multiplier constraint (Martinec 1999), and allows for the presence of internal forcing as specified by the right-hand side of Eq. (5). The magnetic field is parameterized by vector spherical harmonic functions in the angular directions. This approach inherently separates the poloidal and toroidal magnetic field modes and thus can include or suppress energy exchange between the two modes through lateral conductivity variations, as needed. The disadvantage of spherical harmonic functions is that they are susceptible to the Gibbs phenomenon if the expanded function contains discontinuities. The high contrast of electrical conductivity between oceans and continents may thus cause ringing in the computed OIMF. The spatial extension of ringing can be reduced by increasing the spatial resolution. The solver can also solve the stationary problem by simply setting the reciprocal time step to zero. Three-dimensional functions are used for the electrical conductivity and the internal forcing. The two-dimensional approach can be simulated by specifying a layer of small but finite thickness. However, full three-dimensional spatial operators are preserved even in this case.

Both ocean velocities and electrical conductivity values are located at the same grid points. For fast and accurate transformations between the spatial and spherical harmonic domains, we utilize Gauss–Legendre quadrature nodes in colatitude; however, this can introduce small differences due to grid interpolation. The numerical resolution of the method is controlled by the choice of spherical harmonic truncation degree j_{max} and the number of layers k_{max}. The implicit formulation in time leads to a large, block-tridiagonal matrix that needs to be solved at each time step. For lateral resolution up to $j_{\mathrm{max}} \approx 80$ a direct solver based on the factorization of individual blocks is employed. For larger resolutions, the memory requirements do not allow storage of the full matrix, and an iterative

Table 1 Quick comparison of the EM induction solvers used in the study

Solver	Physics	Ocean layer	Sub-ocean layer	Domain	Discretization	
					Lateral	Radial
ElmgTD	Full	3-D	Conductor or insulator	Time	SH	FE
X3DG	Full	3-D	Conductor or insulator	Freq	PWC	PWC
UTSM	UTSA	2-D thin sheet	Insulator	Time	FD+SH	–

UTSA unimodal thin-sheet approximation of Tyler et al. (1997) and Vivier et al. (2004) with insulating mantle and core, *SH* spherical harmonics, *FE* finite elements, *PWC* piece-wise constant representation, *FD* finite differences

Šachl *et al. Earth, Planets and Space*   (2019) 71:58

Page 4 of 13

matrix-free solver must be used in each time step employing a sparse preconditioner based on an a-priori 1-D conductivity model.

X3DG solver

X3DG (Kuvshinov 2008) solves the Maxwell equations (1)–(3) in the frequency domain using the integral equation (IE) approach. Within this approach, the electric/magnetic fields are expressed as a sum of electric/magnetic fields within a background media that has 1-D conductivity and the volume integral of the conductivity anomaly with respect to the background media multiplied by the Greens tensor and the electric field. This system of integral equations is solved iteratively. The construction and calculation of Green's tensors are discussed in detail in Kuvshinov and Semenov (2012). Note that the actual implementation of the IE approach in X3DG is based on the so-called contracting integral equation (CIE, Pankratov et al. 1995; Singer 1995). The advantage of using the CIE is that the condition number of the CIE system matrix depends only on the square root of maximum lateral conductivity contrast in the model (Pankratov and Kuvshinov 2016) and thus does not require preconditioning the matrix.

The X3DG solver computes frequency-domain electric and magnetic fields in spherical Earth models that have 3-D electrical conductivity distribution. Alternatively, infinitesimal sheets with prescribed 2-D conductance can also be used, leading to reduced dimensionality of the corresponding Green tensors. The model allows for excitation in the form of spatially distributed extraneous electric currents either above or within the Earth. The fields can be computed at any point of physical space. The excitation electric current's frequency can be small but must be nonzero. The stationary regime is mimicked with a sufficiently small frequency; in this study, we use 10^{-6} years^{-1}. The solver can account for complex-valued (i.e. for modelling displacement currents and polarization effects), and tensor-valued (i.e. for modelling the effect of anisotropy) electrical conductivities. The X3DG solution contains both the poloidal and the toroidal modes, but their separation is not as straightforward as in ElmgTD.

All electromagnetic fields and 3-D electric conductivity distributions are parameterized within X3DG by piece-wise constant functions in both the angular and radial directions. The grid is assumed to be longitudinally equidistant. Ocean velocities and electrical conductivity values are located at the same grid points. X3DG's computational load (i.e. memory and time of execution) depends linearly on the longitudinal dimension, and quadratically on the latitudinal dimension and on the number of 3-D layers in the model.

UTSM solver

The UTSM solver is based on the unimodal thin-sheet approximation of Tyler et al. (1997) and Vivier et al. (2004). In this approximation, the 3-D EM induction equation is simplified. The self-induction term is neglected. and the equations are vertically integrated. The 3-D problem is thus reduced into a 2-D problem for a thin sheet. Moreover, the thin sheet is assumed to be surrounded by an insulator on the top and bottom, i.e. both outer space and also the Earth's mantle and core are treated as insulators.

Technically, the 3-D EM induction equation is replaced by the simplified 2-D equation for the stream function $\psi(\vartheta, \varphi, t)$ at colatitude ϑ, longitude φ, and time t,

$$\frac{1}{a^2} \nabla_\Omega \cdot \left(\frac{1}{\Sigma} \nabla_\Omega \psi \right) = - \left[\nabla \times \left(\frac{\mathbf{J}^{\mathrm{imp}}}{\Sigma} \right) \right] \cdot \mathbf{e}_r, \qquad (7)$$

where a is the Earth's radius, ∇_Ω is the angular part of the nabla operator, $\mathbf{e}_r$ is the unit radius vector, $\Sigma(\vartheta, \varphi)$ is the vertically integrated conductivity and $\mathbf{J}^{\mathrm{imp}}(\vartheta, \varphi, t)$ is the vertically integrated imposed electric current density,

$$\Sigma(\vartheta, \varphi) = \int\limits_{-h}^{\eta(\vartheta, \varphi)} \sigma(\mathbf{r}) \mathrm{d}r, \qquad (8)$$

$$\mathbf{J}^{\mathrm{imp}}(\vartheta, \varphi) = \int\limits_{-h}^{\eta(\vartheta, \varphi)} \mathbf{j}^{\mathrm{imp}}(\mathbf{r}, t) \mathrm{d}r, \qquad (9)$$

in which $\eta(\vartheta, \varphi)$ is the sea surface height and h is the thickness of the ocean layer. Notice that the radial diffusion term is missing in the stream-function equation. The term on the left-hand side of Eq. (7) resembles the first term on the left-hand side of Eq. (5). However, the term in Eq. (5) contains 3-D spatial operators, while the operators in Eq. (7) are only 2-D.

Equation (7) is discretized by the finite-difference method on a C-grid (Arakawa and Lamb 1977) and its solution is expanded into spherical harmonics. The spherical harmonic coefficients of ψ are converted to the internal-field coefficients of the magnetic field using a simple scaling relation.

Modelling framework

We consider four test cases labelled A–D. We describe our electrical conductivity and ocean circulation models first, discuss how forcing is applied to our EM induction solvers, and finally present the considered test cases.

Šachl *et al. Earth, Planets and Space* (2019) 71:58

Page 5 of 13

Conductivity model

We consider the 3-D conductivity, σ, at a depth h from the sea surface down to the bottom of the ocean layer. Conductivity is determined using the bathymetry $b(\vartheta, \varphi)$,

$$\sigma(r, \vartheta, \varphi) = \begin{cases} \sigma_{\text{ocean}} & \text{for } r \geq a - b(\vartheta, \varphi), \\ \sigma_{\text{crust}} & \text{for } a - h \leq r < a - b(\vartheta, \varphi), \end{cases}$$

where σ_{ocean} and σ_{crust} are the nominal conductivities of sea water and crust. In this study, we use the values,

$$\sigma_{\text{ocean}} = 3.2 \text{ S/m}, \quad a = 6371 \text{ km},$$

$$\sigma_{\text{crust}} = 10^{-3} \text{ S/m}, \quad h = 6 \text{ km}.$$

The bathymetry is reused from the ocean circulation model OMCT, as introduced below. This simplified conductivity model is easy to implement in all used approaches and preserves the dominant effect of laterally varying bathymetry. Note that Velímský et al. (2019) used a salinity and temperature-dependent conductivity with the ElmgTD solver, and the implementation of the recent WOA conductivity from collocated measurements (Tyler et al. 2017) is underway for future studies. In Case A, we
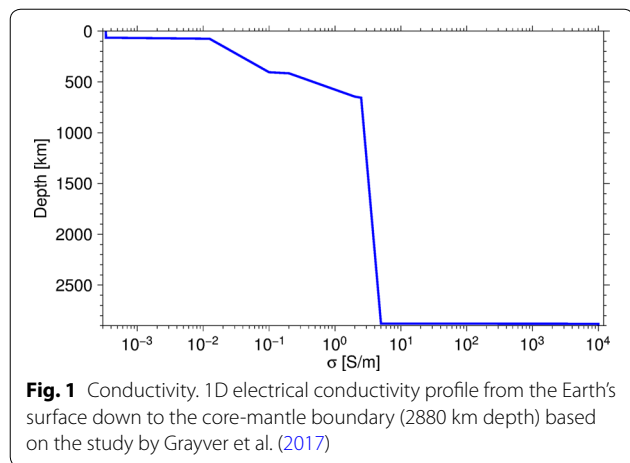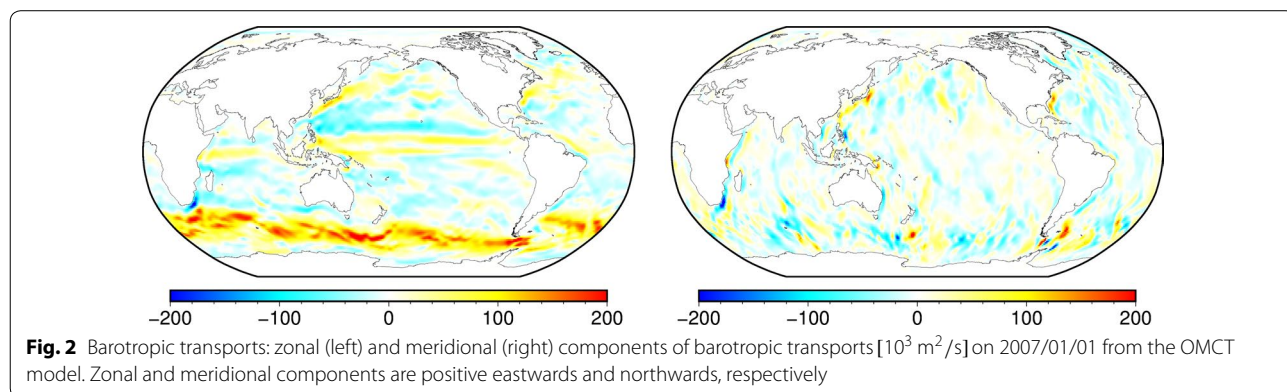
consider both the mantle and the core to be perfect insulators. In the other cases, the mantle conductivity is given by a 1-D profile from Grayver et al. (2017), and the core is considered to be highly conductive (10^4 S/m). The mantle conductivity profile is shown in Fig. 1.

Ocean circulation model

We simulate the general ocean circulation using the Ocean Model for Circulation and Tides (OMCT, Thomas et al. 2001). This model depicts the major ocean currents (Dobslaw et al. 2013) and has already been used for several studies on EM induction in the ocean (Irrgang et al. 2016a, b; Saynisch et al. 2016). The corresponding ocean velocities **u** build the source for ocean circulation's electric currents and the motional induction.

The OMCT is a baroclinic general ocean circulation model that incorporates nonlinear balance equations for momentum, conservation equations for heat and salinity, and the continuity equation. The hydrostatic and the Boussinesq approximations are applied. Artificial mass changes due to the Boussinesq approximation are corrected as proposed by Greatbatch (1994).

We use the configuration in which OMCT is set up on a C-grid (Arakawa and Lamb 1977) with a horizontal resolution of 1°, 20 layers in the vertical, and a time step of 20 minutes (Dobslaw et al. 2013). Ocean tides are not considered. OMCT's bathymetry is based on ETOPO1 (Amante 2009) with local adjustments to keep the natural bathymetric current barriers. We force the ocean model with 3-hourly reanalysis products from the European Centre for Medium-Range Weather Forecasts (ECMWF, Dee et al. 2011), which encompass wind stress, precipitation, evaporation, and surface pressure. As an example, we show the OMCT barotropic transports on 2007/01/01 in Fig. 2.

Fig. 1 Conductivity. 1D electrical conductivity profile from the Earth's surface down to the core-mantle boundary (2880 km depth) based on the study by Grayver et al. (2017)

Fig. 2 Barotropic transports: zonal (left) and meridional (right) components of barotropic transports [10^3 m^2/s] on 2007/01/01 from the OMCT model. Zonal and meridional components are positive eastwards and northwards, respectively

Forcing

We compute the forcing using the OMCT velocities **u** and the 12th generation of the International Geomagnetic Reference Field (IGRF–12, Thébault et al. 2015) $\mathbf{B}_M$. OMCT velocities are bilinearly interpolated from the staggered Arakawa C-grid to the grids required, respectively, by ElmgTD and X3DG. Since the velocity field is primarily large scale, this interpolation is not critical for our study. The UTSM solver is build on the same grid as OMCT, and thus, no interpolation is needed.

The OMCT velocities are provided in 20 layers using partial bottom cells. This method allows the thickness of bottom grid cells to differ from the respective global layer thickness which leads to better representation of bathymetry. For EM induction modelling, we reduce the vertical resolution by merging the OMCT layers into a single layer in Cases A–B, and into five layers in Cases C–D. We use a thickness-weighted averaging scheme that preserves the total transports.

For stationary Cases A–C, we prescribe the forcing using the OMCT velocities on 2007/01/01. For Case D, we use a time series of forcing spanning the years 2004-2007, with a temporal discretization step of one day. The first three years are a spin-up period to suppress the transient effect of initial conditions on the time-domain ElmgTD. Based on our experience, the spin-up is sufficiently long if initial conditions are taken in the form of the static solution.

Test cases

Our study's four test cases are summarized in Table 2. Complexity increases from Case A to Case D. In the simplest Case A, the underlying mantle is treated as a perfect insulator and the ocean has no vertical structure. In ElmgTD and X3DG, we use a single oceanic layer of finite thickness. The UTSM solver uses the equivalent thinsheet set-up. The test case is stationary and calculates a single snapshot corresponding to 2007/01/01. The solution is also unimodal, containing only the poloidal magnetic field.

In Case B, we include the 1-D mantle conductivity model and consider a bimodal solution, the toroidal magnetic field is included. Thus, the ocean and mantle are galvanically coupled through vertical electric currents.

The UTSM is not used anymore, as the physical model is beyond its approximation. The inclusion of galvanic coupling is very cheap for both the ElmgTD and X3DG solvers. The additional cost results in extension of runtime by a few percents.

In Case C, we add the vertical stratification of imposed currents and ocean conductivity, using five layers with lower boundaries at depths of 87.5 m, 187.5 m, 500 m, 1700 m, and 6000 m. Runtimes of both the X3DG and ElmgTD solvers scale up from approximately one hour for Cases A and B to about one day for Case C.

Finally, Case D implements self-induction and we calculate the full time series throughout the year 2007. X3DG could theoretically solve this case by using a Fourier-transformed excitation in the frequency domain, but this is beyond the scope of our study since the OIMF's spectrum is wide ranged and the X3DG computation would be expensive. Given the cross-validation of ElmgTD and X3DG on the static cases, we find it sufficient to use only ElmgTD to evaluate the effect of self-induction.

Our EM solvers are based on different numerical techniques, and thus, the resolution used is not exactly the same. We use 1° resolution in X3DG and UTSM. In ElmgTD, we set up the maximum spherical harmonic degree to $j_{max} = 480$ in Cases A–C in order to minimize the effect of ringing. In Case D, the solution evolves in time which forced us to decrease the resolution to $j_{max} = 80$ in order to enable the use of the ElmgTD direct solver.

Comparison methods

We assess the performance of individual solutions by three methods. The first one is comparing the X, Y, and Z components of the OIMF at the Earth's surface and at the depth of 6 km. The purpose is to visually inspect the key spatial features of the OIMF.

The second method is to compare the power spectrum of OIMF, computed according to Eq. (21) in Maus (2008). We calculate the power spectra at the Earth's surface and at a typical satellite altitude of 400 km.

Finally, for Case D we inspect the time evolution of power P_j on the first four spherical harmonic degrees.

Table 2 Test cases considered in the study

Case	Mantle + core	Galvanic coupling	Ocean layers	Self-induction	EM solvers used
A	Insulator	No	1	No	ElmgTD, X3DG, UTSM
B	1D	Yes	1	No	ElmgTD, X3DG
C	1D	Yes	5	No	ElmgTD, X3DG
D	1D	Yes	5	Yes	ElmgTD

Results

Case A

We depict the computed OIMFs at the Earth's surface in Fig. 3. Regardless of the solver used, the largest amplitudes of the OIMF are located in the region of the Antarctic Circumpolar Current (ACC), which agrees with other studies (e.g. Manoj et al. 2006). The Z component is somewhat stronger than the X and Y components, although it does not dominate the other two. The minimum values of the X, Y, and Z components in the ElmgTD solution are -2.14 nT, -4.13 nT, and -5.87 nT, respectively. The maximum values of the X, Y, and Z components in the ElmgTD solution are 2.68 nT, 2.28 nT, and 4.56 nT, respectively. Considering the structure of the OIMF, the Y component is the most complex. Its minima and maxima frequently alternate, especially in the ACC region of the Indian Ocean between Africa and Australia. The Z component is less complicated; it is predominantly positive in the Indian Ocean and predominantly negative in the South Pacific.

There is a good agreement between the ElmgTD and X3DG solutions. The large-scale patterns agree well; however, some discrepancies exist in the smaller-scale structures. In accordance, the power spectra depicted in Fig. 4 match for the lower degrees but disagree for the
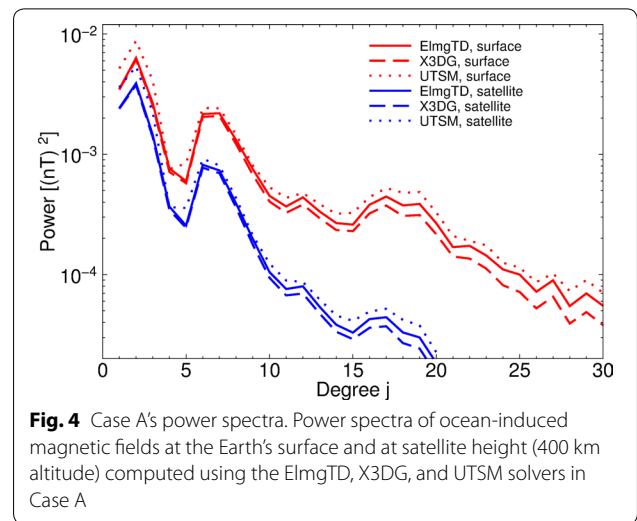
Fig. 4 Case A's power spectra. Power spectra of ocean-induced magnetic fields at the Earth's surface and at satellite height (400 km altitude) computed using the ElmgTD, X3DG, and UTSM solvers in Case A

higher degrees. The level of discrepancy also depends on the lateral resolution since ElmgTD and X3DG solvers have different sensitivity to the resolution. If we decrease the lateral resolution from $1°$ to $2°$ in X3DG and from $j_{max} = 480$ to $j_{max} = 80$ in ElmgTD, the ElmgTD power spectrum slightly changes, but the X3DG power
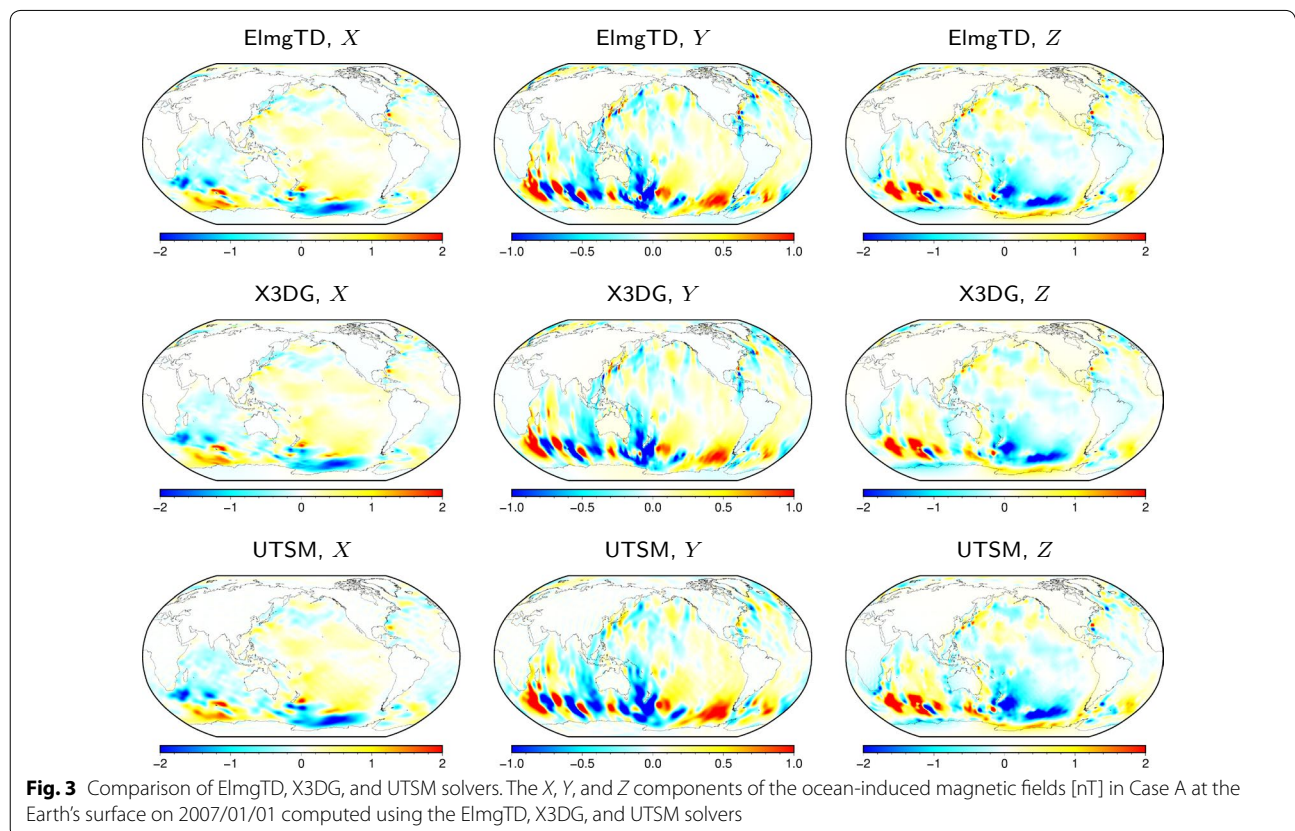

Fig. 3 Comparison of ElmgTD, X3DG, and UTSM solvers. The X, Y, and Z components of the ocean-induced magnetic fields [nT] in Case A at the Earth's surface on 2007/01/01 computed using the ElmgTD, X3DG, and UTSM solvers

Šachl *et al. Earth, Planets and Space*   (2019) 71:58

Page 8 of 13

spectrum drops significantly—only the lowest degrees are minimally unaffected (see Fig. 5). We attribute the discrepancies and the varying sensitivity to the different numerical methods used. The CIE method used in the X3DG solver allows for a more local representation of the magnetic field than does the spherical harmonics used in the ElmgTD solver. However, the spherical harmonics' behaviour is not necessarily a disadvantage as long as the main modelling task is to compute the global solution with its large-scale features. Spherical harmonics are well suited for global studies but if fine-scale features are of paramount importance, the X3DG solver would be the better choice.

The UTSM solution agrees qualitatively with the ElmgTD and X3DG solutions. Nonetheless, a more detailed inspection reveals differences in the spatial patterns of its OIMF: its amplitudes are larger and the UTSM spectrum (shown in Fig. 4) is above the ElmgTD and X3DG spectra for all the considered degrees. These differences are likely due to the unimodal thin-sheet approximation's assumption that each of the OIMF's X and Y components has equal magnitude, but opposite

Fig. 5 Effect of lateral resolution. Power spectra of ocean-induced magnetic fields at the Earth's surface in Case A computed with the ElmgTD solver using $j_{max} = 80$ and $j_{max} = 480$ and X3DG solver using 1° and 2° lateral resolutions

sign, just above and below the thin ocean layer. This assumption is correct for an infinitely thin sheet surrounded by an insulator, but it is incorrect for a thin spherical shell. One can show that the spherical harmonic coefficients of the horizontal magnetic field in the insulators just above and under the thin spherical shell are related by a $-j/(j+1)$ ratio. Hence, substantial errors are introduced for the large-scale magnetic fields, while the small-scale features are well represented by the UTSM. Currently, this problem can be addressed by an improved method, such as that given in Eq. (2.42) of Tyler et al. (2017).

In order to complete our analysis of Case A, we depict the power spectra and spatial patterns of the OIMF at the satellite level in Figs. 4 and 6, respectively. The OIMF in the atmosphere decreases with r according to $r^{-(j+2)}$ and the power for degree j decreases as $r^{-(2j+4)}$. Thus, short wavelengths are damped more rapidly than long wavelengths. Consequently, the spectrum of OIMF at satellite altitude decays faster and its spatial patterns are much smoother than spatial patterns computed at the Earth's surface (compare Figs. 3 and 6).

In the remaining test cases, we only discuss the OIMF computed by the ElmgTD solver. Nonetheless, we still compare the ElmgTD and X3DG spectra to ensure that both solvers respond similarly.
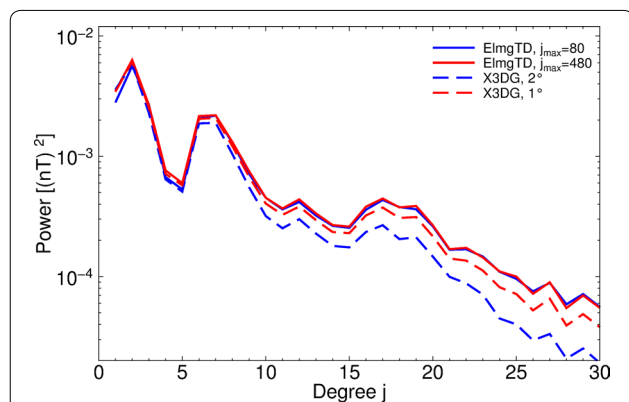
Case B

Figure 8 depicts the differences between Case B's and Case A's OIMFs computed at the Earth's surface using the ElmgTD solver. There are significant changes in the OIMF due to the added effect of galvanic coupling. Although the toroidal mode's amplitude is equal to zero at the Earth's surface, it is nonzero inside the Earth (Velímský et al. 2019) and there is coupling between the toroidal and poloidal field components. The toroidal mode is converted to the poloidal mode by the lateral electrical conductivity variations. Consequently, the toroidal mode affects the poloidal mode at the Earth's
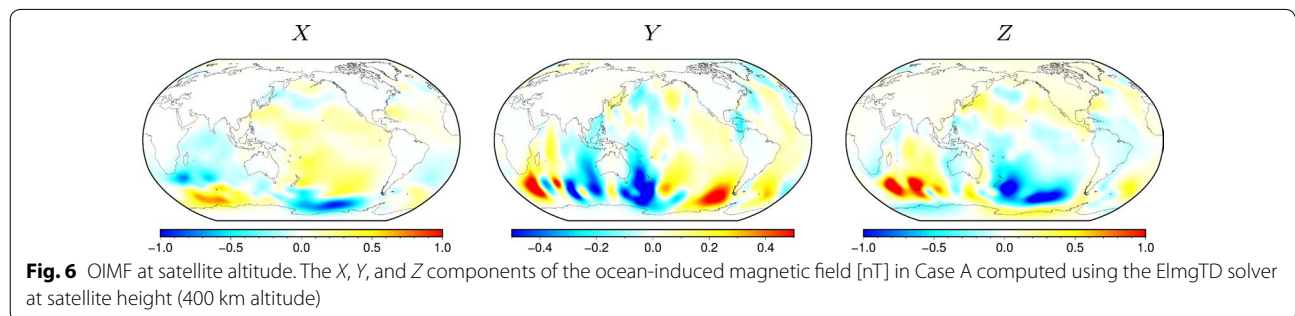

Fig. 6 OIMF at satellite altitude. The *X*, *Y*, and *Z* components of the ocean-induced magnetic field [nT] in Case A computed using the ElmgTD solver at satellite height (400 km altitude)

Šachl *et al. Earth, Planets and Space*   (2019) 71:58

Page 9 of 13

surface even though the toroidal mode itself has zero amplitude there.

Based on Fig. 8, the OIMF in Case B is stronger in some regions than the OIMF in Case A, but the opposite is the case in other regions. The power spectra (compared in Fig. 7) are more instructive. Indeed, Case B's OIMF has less power for degrees higher than five, but it has more power for degrees one to five. Degree one is especially stronger; its power has increased from 1.8×10^{-2} $(nT)^2$ to 1.1×10^{-1} $(nT)^2$. The shift of the power spectra is consistent in both ElmgTD and X3DG solutions (compare the full and dashed red lines with the full and dashed blue lines in Fig. 7). A similar power spectra shift was
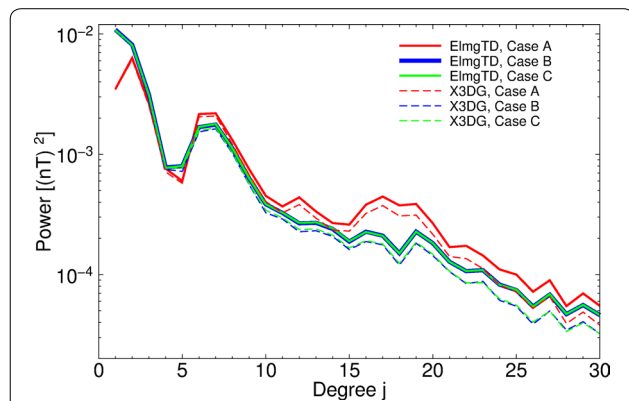

Fig. 7 Effect of different physical approximations on the OIMF power spectra. Power spectra of the ocean-induced magnetic fields computed using the ElmgTD solver (solid line) and the X3DG solver (dashed line) in Cases A–C at the Earth's surface

theoretically predicted by Tyler (2017) and reported by Velímský et al. (2018) for the magnetic field driven by ocean tides. These studies predicted the critical crossover degree would be six rather than five.

Figure 9 shows the differences between OIMFs from the same cases as in Fig. 8 but at the bottom of the surface layer (i.e. 6 km deep) rather than at the Earth's surface. The sensitivity of individual OIMF components to galvanic coupling differs—the Z component is the least sensitive, whereas the Y component is the most sensitive. Indeed, the Y component's amplitudes have significantly increased due to the toroidal mode; the Y component plot's colour scale maximum value is now 10x larger. Besides changing the magnitude of the Y component, the spatial pattern has also changed. At this depth, Case B's Y component is positive for the entire ACC region—Case A's spatially alternating positive and negative amplitude regions are no longer visible.

Case C

The vertical stratification of flow and conductivity has much less impact on the OIMF than the inclusion of galvanic coupling. Case B's and Case C's power spectra are virtually identical for both ElmgTD and X3DG solutions (see Fig. 7). In fact, the effect of vertical stratification is negligible for most of the globe; however, there are certain regions where vertical stratification matters—for example, coastal areas around New Zealand, north of the Bahama Islands, and south of Japan, see Figs. 8 and 9. These areas have differences in the surface Z component up to 1.1 nT. Thus, for comparing modelled OIMF
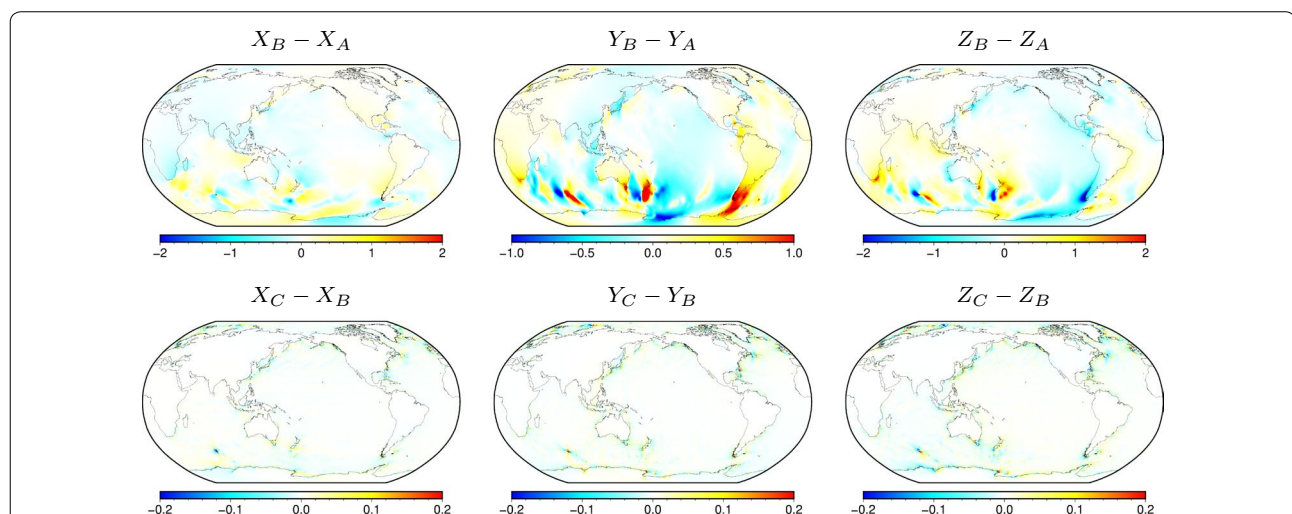

Fig. 8 Effect of galvanic coupling (Case B) and vertical stratification (Case C) on the OIMF at the Earth's surface The top row shows the differences [nT] between Cases B and A in the *X*, *Y*, and *Z* components of the ocean-induced magnetic fields computed using the ElmgTD solver. The bottom row shows the differences between the OIMFs in Cases C and B
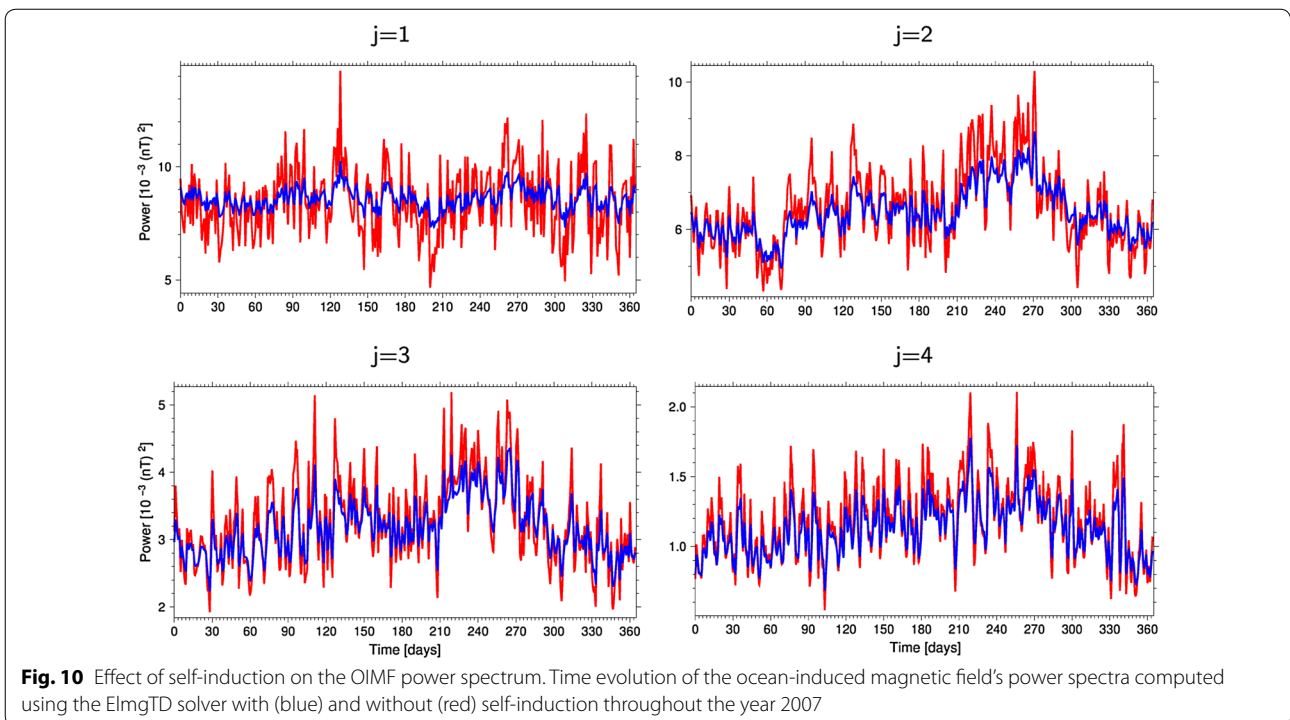
Fig. 9 Effect of galvanic coupling (Case B) and vertical stratification (Case C) on the OIMF at 6 km depth. The top row shows the differences [nT] between Cases B and A in the *X*, *Y*, and *Z* components of the ocean-induced magnetic fields computed using the ElmgTD solver. The bottom row shows the differences between OIMFs in Cases C and B
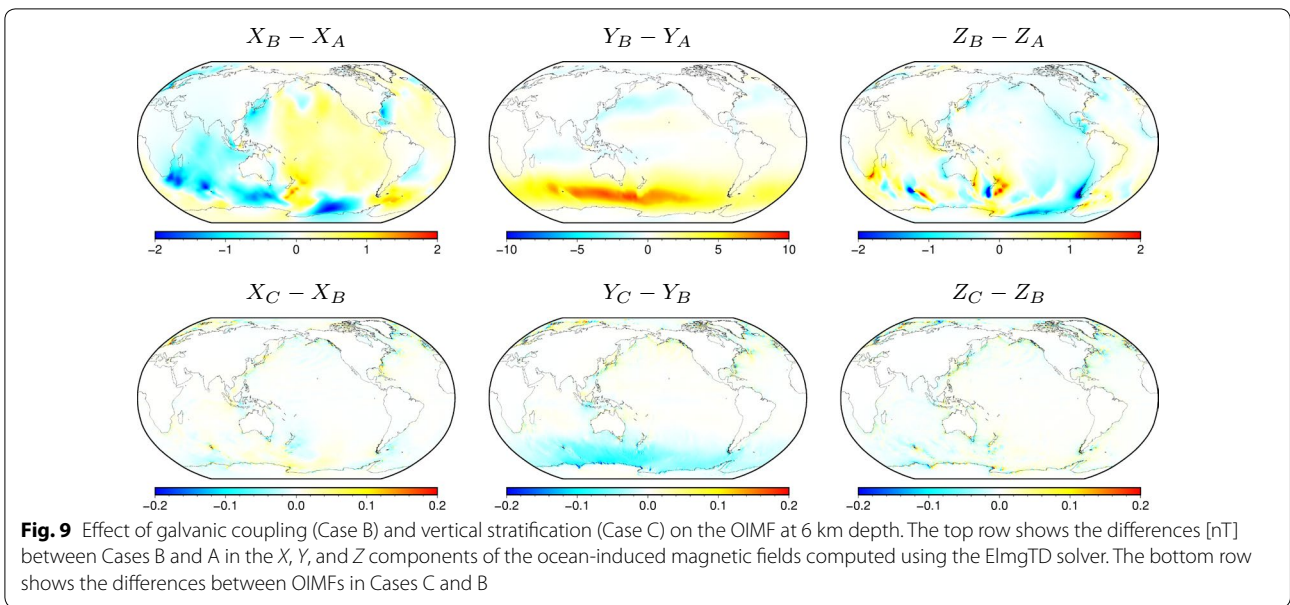
to measurement from coastal stations, using the full 3-D approach should provide a more accurate comparison.

Case D

Figure 10 shows the effect of self-induction on the spectral power of low degrees (1-4). The red curve represents the time evolution of spectral power computed without the self-induction term (which corresponds to Case C's configuration), while the blue curve represents the time evolution of spectral power with the self-induction term included. The red curve is obviously oscillating more rapidly than the blue curve. The difference between the two spectra is largest for the lowest degree $j = 1$; the difference is much weaker

Fig. 10 Effect of self-induction on the OIMF power spectrum. Time evolution of the ocean-induced magnetic field's power spectra computed using the ElmgTD solver with (blue) and without (red) self-induction throughout the year 2007

for $j = 4$ and it further diminishes for higher degrees (not shown). Otherwise, the mean evolution trajectories of both solutions are similar, suggesting that the self-induction term damps the solution's fast temporal oscillations, smoothing the time evolution. Additionally, the solution computed without the self-induction term follows the forcing instantly, while the solution that contains the self-induction term is delayed in time. Cross-correlating the spherical harmonic coefficients from the two solutions, we determined that the time delay is not the same for all coefficients. Coefficients $(j = 1, m = -1)$, $(2, -2)$, $(2, 2)$, $(3, -3)$, $(3, 0)$, $(3, 1)$ and $(5, -3)$ show the largest delay of 5 h. The general tendency is that the delay decreases with the increasing spherical harmonic coefficient degree, e.g. the largest delay among the $j = 10$ coefficients is 2 hours.

The error caused by the neglection of the self-induction term is evidently time-dependent. We compare the OIMFs computed with and without the self-induction term for time $t = 1$ day and $t = 128$ days. The latter time instant corresponds to the largest difference in spectral power on degree one, i.e. $\Delta P_1 = |(P_1)_D - (P_1)_C| = 4.5 \times 10^{-3}$ (nT)^2. Figure 11 shows the OIMF differences between the Case D and Case C solutions both using $j_{max} = 80$. Their spatial pattern is predominantly large-scale which corresponds to the above-mentioned fact that the spectral powers most differ for the lowest degrees. The amplitudes of the differences do not exceed 10% of the signal strengths, and there are no specific regions in which the differences are more pronounced.

Conclusions

In this paper, we study the effects of various physical and numerical approximations commonly used in the modelling of the ocean-induced magnetic field (OIMF). We formulate four test cases with increasing complexity and use three well-established EM induction solvers—ElmgTD, X3DG and UTSM—for this purpose.

Our computations suggest that the unimodal solution is insufficient for modelling the OIMF due to the absence of galvanic coupling. Galvanic coupling significantly alters the OIMF power spectrum as well as its spatial pattern at the Earth's surface. The most striking feature is the Y component's change in amplitude at the bottom of the surface layer (6 km depth) due to including the toroidal mode. Its spatial pattern is completely different, the values in the region of the Antarctic Circumpolar Current become only positive, and the maximum amplitudes are approximately one order of magnitude larger than in the galvanically decoupled case.

The self-induction term is less important; however, it has a time-dependent smoothing effect on the solution in time, which causes the magnetic field to oscillate less rapidly. Self-induction substantially affects the lowest degrees—the power on degree one may increase/decrease by 40% at the surface. The higher degrees are influenced much less; for instance, the power on degree ten may increase/decrease by 10%. The overall maximum change in the OIMF is around 0.1 nT in the X and Y components and 0.15 nT in the Z component. With respect to future efforts to recover the OIMF from Swarm satellite data, our analysis yields a mildly optimistic outlook. Self-induction reduces the fast time variations of the large-scale signatures represented by

Fig. 11 Effect of self-induction on the OIMF at the Earth's surface. Differences [nT] between the ocean-induced magnetic fields at the Earth's surface computed using the ElmgTD solver with (Case D) and without (Case C) self-induction on 2007/01/01 and 2007/05/08

Šachl *et al. Earth, Planets and Space*   (2019) 71:58

Page 12 of 13
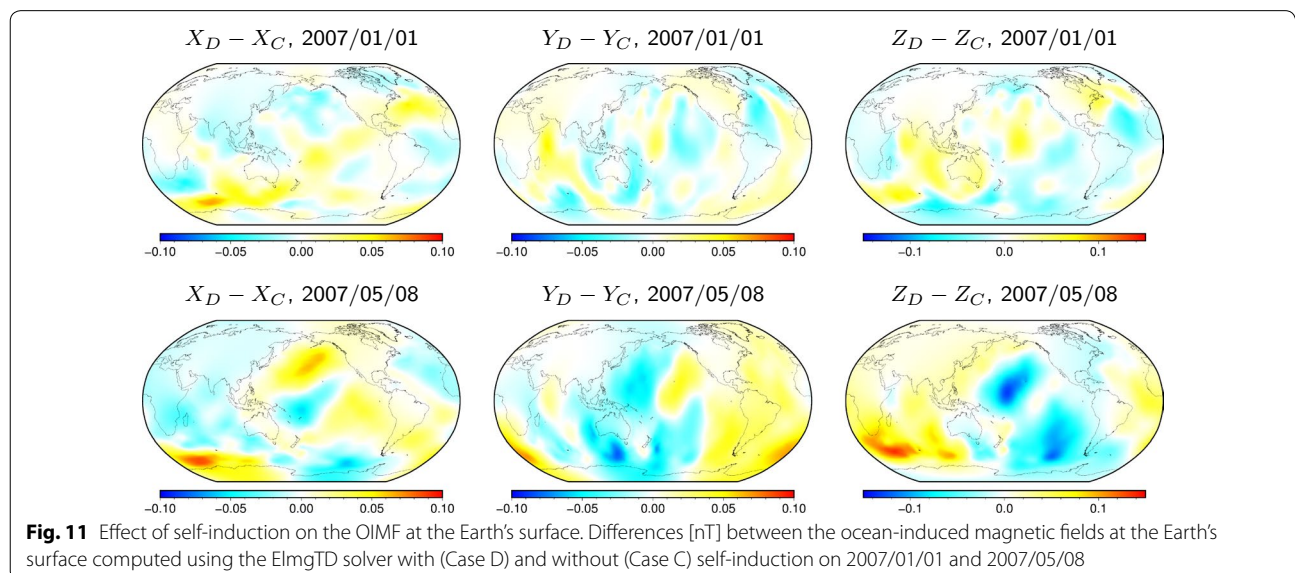
the low-degree spherical harmonic coefficients, which are potentially observable by satellite measurements. This could be exploited through stacking techniques in analysing Swarm data. On the other hand, seasonal variations are still preserved in the predicted low-degree signals and thus remain potentially exploitable for the remote sensing of ocean flow changes.

The vertical stratification of flow and electrical conductivity matters for local modelling of the OIMF; some localities experience differences in amplitude over 30%. For global studies, the increased vertical resolution is unnecessary and a bimodal solution calculated using one ocean layer sufficiently captures the global pattern of the OIMF.

Finally, a horizontal resolution of at least $1°$ is recommended. Our models exhibit unwanted divergence when coarser ($2°$) resolution was used.

Consequently, the unimodal thin-sheet approximation of Tyler et al. (1997) and Vivier et al. (2004) seems to be too crude of an approximation of the governing equations since it neglects both the galvanic coupling and self-induction terms. It might be suitable for some parametric studies due to its reduced computational costs, but we hesitate to recommend it if accuracy matters.

Author details
[1] Department of Geophysics, Faculty of Mathematics and Physics, Charles University, V Holešovičkách 2, 180 00 Praha 8, Czech Republic. [2] Dublin Institute for Advanced Studies, 5 Merrion Square, Dublin 2, Ireland. [3] Section 1.3, Earth System Modelling, Helmholtz Centre Potsdam, GFZ German Research Centre for Geosciences, Potsdam, Germany. [4] Department of Geological Sciences/CIRES, University of Colorado, Boulder, CO, USA.

References
Amante C (2009) ETOPO1 1 arc-minute global relief model: procedures, data sources and analysis. NOAA Technical Memorandum NESDIS NGDC-24, National Geophysical Data Center, NOAA, Boulder, Colorado. http://www.ngdc.noaa.gov/mgg/global/global.html. Accessed 14 May 2019

Arakawa A, Lamb VR (1977) Computational design of the basic dynamical processes of the UCLA general circulation model. Methods Comput Phys 17:173–265

Cox CS, Filloux JH, Larsen JC (1970) Electromagnetic studies of ocean currents and electrical conductivity below the ocean floor. Sea 4:637–693

Dee DP, Uppala SM, Simmons AJ, Berrisford P, Poli P, Kobayashi S, Andrae U, Ma Balmaseda, Balsamo G, Bauer P, Bechtold P, Beljaars ACM, van de Berg L, Bidlot J, Bormann N, Delsol C, Dragani R, Fuentes M, Geer AJ, Haimberger L, Healy SB, Hersbach H, Hólm EV, Isaksen L, Kaallberg P, Köhler M, Matricardi M, McNally AP, Monge-Sanz BM, Morcrette J-J, Park B-K, Peubey C, de Rosnay P, Tavolato C, Thépaut J-N, Vitart F (2011) The ERA-Interim reanalysis: configuration and performance of the data assimilation system. Q J R Meteorol Soc 137(656):553–597. https://doi.org/10.1002/qj.828

Dobslaw H, Flechtner F, Bergmann-Wolf I, Dahle C, Dill R, Esselborn S, Sasgen I, Thomas M (2013) Simulating high-frequency atmosphere-ocean mass variability for dealiasing of satellite gravity observations: AOD1B RL05. J Geophys Res 118(7):3704–3711. https://doi.org/10.1002/jgrc.20271

Flosadóttir AH, Larsen JC, Smith JT (1997) Motional induction in North Atlantic circulation models. J Geophys Res Oceans 102(C5):10353–10372

Friis-Christensen E, Lühr H, Hulot G (2006) Swarm: a constellation to study the Earth's magnetic field. Earth Planets Space 58(4):351–358. https://doi.org/10.1186/BF03351933

Grayver A, Munch F, Kuvshinov A, Khan A, Sabaka T, Tøffner-Clausen L (2017) Joint inversion of satellite-detected tidal and magnetospheric signals constrains electrical conductivity and water content of the upper mantle and transition zone. Geophys Res Lett 44:6074–6081

Greatbatch RJ (1994) A note on the representation of steric sea level in models that conserve volume rather than mass. J Geophys Res 99(C6):12767. https://doi.org/10.1029/94JC00847

Irrgang C, Saynisch J, Thomas M (2016a) Ensemble simulations of the magnetic field induced by global ocean circulation: estimating the uncertainty. J Geophys Res Oceans 121(3):1866–1880. https://doi.org/10.1002/2016JC011633

Irrgang C, Saynisch J, Thomas M (2016b) Impact of variable seawater conductivity on motional induction simulated with an ocean general circulation model. Ocean Sci 12(4):129–136. https://doi.org/10.5194/os-12-129-2016

Irrgang C, Saynisch J, Thomas M (2017) Utilizing oceanic electromagnetic induction to constrain an ocean general circulation model: a data assimilation twin experiment. J Adv Model Earth Syst https://doi.org/10.1002/201simu7MS000951

Kelbert A, Kuvshinov A, Velímský J, Koyama T, Ribaudo J, Sun J, Martinec Z, Weiss CJ (2014) Global 3-D electromagnetic forward modelling: a benchmark study. Geophys J Int 197(2):785–814

Kuvshinov A (2008) 3-D global induction in the oceans and solid Earth: recent progress in modeling magnetic and electric fields from sources of magnetospheric, ionospheric and oceanic origin. Surv Geophys 29:139–186

Kuvshinov AV, Semenov AA (2012) Global 3-D imaging of mantle electrical conductivity based on inversion of observatory C-responses—I. An approach and its verification. Geophys J Int 189:1335–1352

Šachl *et al. Earth, Planets and Space*   (2019) 71:58

Page 13 of 13

Large WG, Yeager SG (2004) Diurnal to decadal global forcing for ocean and sea-ice models: the data sets and flux climatologies. Technical report, National Center for Atmospheric Research Boulder

Large WG, Yeager S (2009) The global climatology of an interannually varying air-sea flux data set. Clim Dyn 33(2–3):341–364

Larsen JC, Sanford TB (1985) Florida current volume transports from voltage measurements. Science 227(4684):302–304

Madec G, Delecluse P, Imbard M, Le'vy C (1998) OPA 8.1 ocean general circulation model reference manual. Note du pôle de modélisation, Inst. Pierre-Simon Laplace, Paris, France

Manoj C, Kuvshinov A, Maus S, Lühr H (2006) Ocean circulation generated magnetic signals. Earth Planets Space 58(4):429–437. https://doi.org/10.1186/BF03351939

Marshall J, Adcroft A, Hill C, Perelman L, Heisey C (1997) A finite-volume, incompressible Navier Stokes model for studies of the ocean on parallel computers. J Geophys Res Oceans 102(C3):5753–5766

Marsland SJ, Haak H, Jungclaus JH, Latif M, Röske F (2003) The Max-Planck-Institute global ocean/sea ice model with orthogonal curvilinear coordinates. Ocean Model 5(2):91–127

Martinec Z (1999) Spectral-finite element approach to three-dimensional electromagnetic induction in a spherical Earth. Geophys J Int 136:229–250

Maus S (2008) The geomagnetic power spectrum. Geophys J Int 174(1):135–142

Oberhuber JM (1993a) The OPYC ocean general circulation mode. Tech. Rep. 7, Dtsh. Klimarechenzentrum GmbH, Hamburg, Germany

Oberhuber JM (1993b) Simulation of the Atlantic circulation with a coupled sea ice-mixed layer-isopycnal general circulation model. Part I: model description. J Phys Oceanogr 23(5):808–829

Olsen N, Stolle C, Floberghagen R, Hulot G, Kuvshinov A (2016) Special issue Swarm science results after 2 years in space. Earth Planets Space 68:172. https://doi.org/10.1186/s40623-016-0546-6

Pankratov O, Kuvshinov A (2016) Applied mathematics in EM studies with special emphasis on an uncertainty quantification and 3-D IE modelling. Surv Geophys 37:109–147

Pankratov O, Avdeev D, Kuvshinov A (1995) Electromagnetic field scattering in a homogeneous Earth: a solution to the forward problem. Phys Solid Earth 31:201–209

Sanford TB (1971) Motionally induced electric and magnetic fields in the sea. J Geophys Res 76(15):3476–3492

Sanford TB (1982) Temperature transport and motional induction in the Florida current. J Mar Res 40:621–639

Saynisch J, Petereit J, Irrgang C, Kuvshinov A, Thomas M (2016) Impact of climate variability on the tidal oceanic magnetic signal—a model-based sensitivity study. J Geophys Res Oceans 121(8):5931–5941. https://doi.org/10.1002/2016JC012027

Singer BS (1995) Method for solution of Maxwell's equations in non-uniform media. Geophys J Int 120(3):590–598

Stephenson D, Bryan K (1992) Large-scale electric and magnetic fields generated by the oceans. J Geophys Res Oceans 97(C10):15467–15480

Thébault E, Finlay CC, Beggan CD, Alken P, Aubert J, Barrois O, Bertrand F, Bondar T, Boness A, Brocco L et al (2015) International geomagnetic reference field: the 12th generation. Earth Planets Space 67:1–19. https://doi.org/10.1186/s40623-015-0228-9

Thomas M, Sündermann J, Maier-Reimer E (2001) Consideration of ocean tides in an OGCM and impacts on subseasonal to decadal polar motion excitation. Geophys Res Lett 28(12):2457–2460. https://doi.org/10.1029/2000GL012234

Tyler RH (2017) Mathematical modeling of electrodynamics near the surface of Earth and planetary water worlds. Technical Report TM-2017-219022, NASA. https://ntrs.nasa.gov/archive/nasa/casi.ntrs.nasa.gov/20170011279.pdf. Accessed 14 May 2019

Tyler RH, Mysak LA, Oberhuber JM (1997) Electromagnetic fields generated by a three dimensional global ocean circulation. J Geophys Res Oceans 102(C3):5531–5551

Tyler RH, Boyer TP, Minami T, Zweng MM, Reagan JR (2017) Electrical conductivity of the global ocean. Earth Planets Space 69:156. https://doi.org/10.1186/s40623-017-0739-7

Velímský J (2013) Determination of three-dimensional distribution of electrical conductivity in the Earth's mantle from Swarm satellite data: time-domain approach. Earth Planets Space 65:1239–1246. https://doi.org/10.5047/eps.2013.08.001

Velímský J, Martinec Z (2005) Time-domain, spherical harmonic-finite element approach to transient three-dimensional geomagnetic induction in a spherical heterogeneous Earth. Geophys J Int 160:81–101

Velímský J, Grayver A, Kuvshinov A, Šachl L (2018) On the modelling of M_2 tidal magnetic signatures: effects of physical approximations and numerical resolution. Earth Planets Space 70:70–192. https://doi.org/10.1186/s40623-018-0967-5

Velímský J, Šachl L, Martinec Z (2019) The global toroidal magnetic field generated in the Earth's oceans. Earth Planet Sci Lett 509:47–54. https://doi.org/10.1016/j.epsl.2018.12.026

Vivier F, Maier-Reimer E, Tyler RH (2004) Simulations of magnetic fields generated by the Antarctic Circumpolar Current at satellite altitude: can geomagnetic measurements be used to monitor the flow? Geophys Res Lett 31(10):L09315

Webb DJ, De Cuevas, BA, Coward AC (1998) The first main run of the OCCAM global ocean model. Internal document 34, Southampton Ocenog. Cent., Southampton, England, UK

Publisher's Note